12th International Symposium on Turbulence and Shear Flow Phenomena (TSFP12)
Osaka, Japan (Online), July 19-22, 2022

INVESTIGATION ON THE DRAG FORCE AND FLOW FIELD OF AN ACCELERATING PLATE

Jesse Reijtenbagh
Laboratory for Aero- and Hydrodynamics
Delft University of Technology
Mekelweg 2, 2628 CD Delft
j.reijtenbagh@tudelft.nl

Mark J. Tummers
Laboratory for Aero- and Hydrodynamics
Delft University of Technology
Mekelweg 2, 2628 CD Delft
m.j.tummers@tudelft.nl

Jerry Westerweel
Laboratory for Aero- and Hydrodynamics
Delft University of Technology
Mekelweg 2, 2628 CD Delft
j.westerweel@tudelft.nl

ABSTRACT

We present results on the instantaneous drag force acting on a rectangular plate that accelerates in a direction normal to the plate surface. Conventionally the drag force on an accelerating object is divided into a steady state term and an added mass term, which can both be time-dependent. However, for prolonged accelerations this theory does not hold. This paper shows a different method to scale the forces that act on an accelerating plate. We base this scaling on an experiment in which a plate was accelerated from rest through a water tank using an industrial gantry robot. In this experiment both the forces that act on the plate and the velocity fields, using PIV, were measured for a large range of accelerations and final velocities. The vorticity fields, obtained from the velocity fields, qualitatively show the same process of vortex formation across the whole range of accelerations. However, the instantaneous drag force and total circulation clearly differ for different accelerations. Shortly after the acceleration period ends, and the plate reaches its final velocity, the drag force and the circulation for different accelerations coincide and do not depend on the acceleration history anymore. We divided the force into two components: the steady state force, which can be scaled by using the drag coefficient, and an instationary force, for which we found a new scaling. This scaling, which involves the square root of both the velocity and the acceleration, can predict the instationary force significantly better than the conventional scaling.

INTRODUCTION

The investigation of an accelerating plate already goes back to the work of Prandtl and has recently gained interest in applications such biological propulsion (for example Weymouth & Triantafyllou (2013); Rival *et al.* (2009)), rowing propulsion (Grift *et al.*, 2019) and flight (Mancini *et al.*, 2015; Mulleners *et al.*, 2017). Although the research on accelerating plates spans many years, it is not exactly clear how acceleration affects the instantaneous lift or drag forces. Conventionally, "hydrodynamic" or "added" mass is considered. However, Leonard & Roshko (2001) state that the added mass is derived from irrotational flow and it is not fully known to what extent it is applicable in other flows, such as separated flows. As multiple experiments, such as from Fernando *et al.* (2020), show that added mass does not fully explain the force that acts on an object due to acceleration, we will take a closer look into the role of acceleration on the drag force of an accelerated plate.

In our experiments the flow field was measured simultaneously to the drag force to determine relevant flow phenomena that contribute to the drag force. This work is a continuation of the investigation of Grift *et al.* (2019) on the drag force on an accelerating submerged plate as a function of the distance from the free surface. The present study considers a larger range of accelerations, final velocities, and distances over which the plate is accelerated. The plate in the present experiment is fully submerged and free-surface effects do not play a role.

EXPERIMENTAL SETUP

The experimental setup is shown in Figure 1. It shows a water filled glass tank with dimensions $2.0\ \mathrm{m} \times 2.0\ \mathrm{m} \times 0.6\ \mathrm{m}$. The plate dimensions are $\ell_a \times \ell_b \times \ell_c = 0.2\ \mathrm{m} \times 0.1\ \mathrm{m} \times 0.004\ \mathrm{m}$. The height of the plate (ℓ_b) is used as the characteristic length scale in this study, in correspondence to the work of Grift *et al.* (2019). An industrial gantry robot (Reis RL50) is used to move the plate through the water. The top of the plate is 0.15 m below the free surface, which is sufficient for the free surface not to affect the drag force on the plate (Grift *et al.*, 2019). Between the robot and the plate a force/torque transducer (ATI Gamma SI 32-2.5) is installed that samples the drag force at 10 kHz. The experiments are done for a range of accelerations, a, and final velocities, V, as listed in Table 1. This range resulted in Reynolds numbers, based on the final velocity V and the plate height ℓ_b, between $Re = 15 \times 10^3$ and $Re = 135 \times 10^3$, which is well into the turbulent regime. The results reported here focus on accelerations between $a = 0.10\ \mathrm{m/s^2}$ and $a = 1.64\ \mathrm{m/s^2}$ towards a final velocity of $V = 0.45\ \mathrm{m/s}$, which is equivalent to a Reynolds number of $Re = 45 \times 10^3$. Instantaneous veloc-

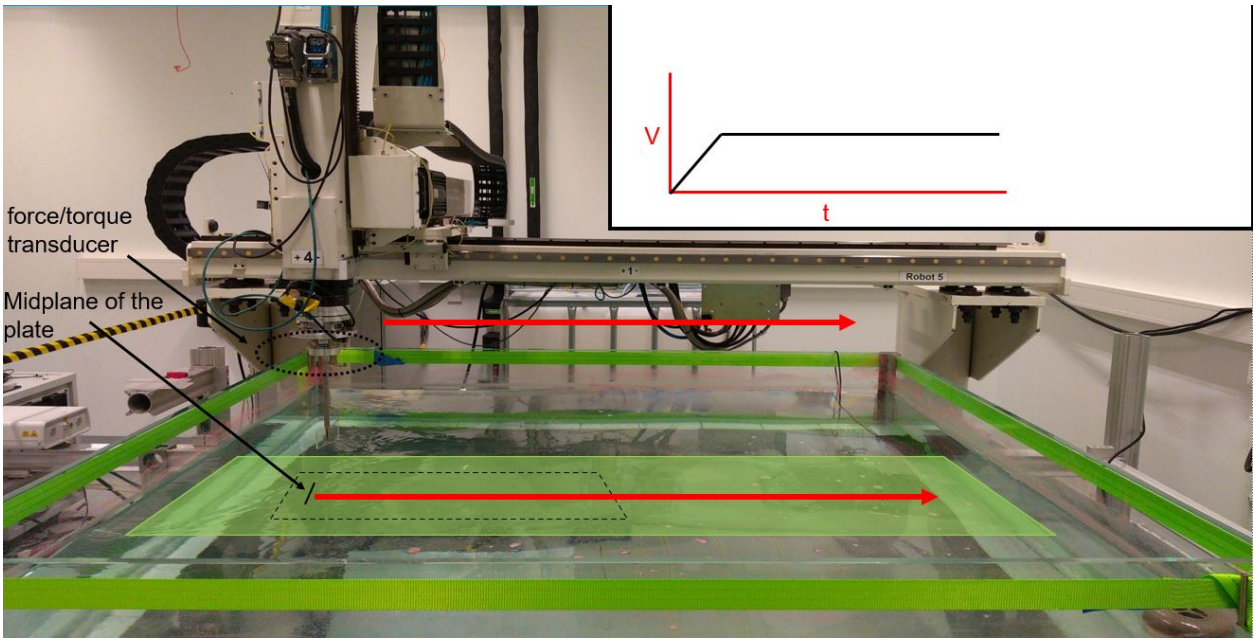

Figure 1. Picture of the experimental setup. The gantry robot moves the plate from left to right, following the red arrow. From the robot head downwards, the following items are attached: a force/torque transducer, a streamlined strut, and the rectangular plate. The laser sheet comes from the left and the camera is located below the tank. The green area indicates the position of the laser sheet, with the field-of-view of the camera indicated by the dashed black area. The horizontal midplane of the plate is indicated by the black line within the field-of-view. The inset graph shows the plate velocity profile as a function of time.

ity fields are measured using a PIV system that is based on a dual cavity Nd:YLF laser (Litron 150W LDY303 HE-PIV) and a 4 megapixel high-speed camera (Phantom VEO 640L). Neutrally buoyant fluorescent spheres (Cospheric UVPMS-BR-0.995) with approximately 60 μm diameter are used as tracer particles. The high-speed camera was equipped with a long-pass filter (Schott OG570) to remove environmental light. Images of the particles were recorded from a field-of-view of 900 mm $\times$ 472 mm. The images were processed in DaVis-10 using a sliding sum-of-correlation method starting with a first pass with a 48$\times$48 pixel interrogation window, followed by three 24$\times$24 pixel passes with a 50% overlap. This resulted in a time-resolved velocity field of 115$\times$219 velocity vectors taken at 1000 Hz. PIV measurements are done for $a = 0.21$ m/s^2 and higher.

FORCE MEASUREMENTS

Figure 2 shows five repetitions of the force signal $F_x(t)$ for the same experimental parameters ($a = 0.82$ m/s^2 and $V = 0.45$ m/s). This shows that the drag force signal reproduces very well over multiple repetitions. The force signal increases during the acceleration phase and reaches a peak value at the end of this phase when the plate assumes its final velocity. The drag force then enters a transition phase towards the steady state phase where the drag force F_{CD} given by:

$$F_{CD} = \tfrac{1}{2} C_D \rho A V^2, \tag{1}$$

where ρ is the fluid density, A $(= \ell_a \times \ell_b)$ the frontal area of the plate, V the velocity of the plate, and C_D the steady state drag coefficient, which was found to be equal to 1.3 in our experiments. The transition from peak drag force to steady state is described in detail by Grift *et al.* (2019). In their research, the peak force is modelled as the sum of this steady state drag force F_{CD}, the force due to the acceleration of the plate mass F_{mp} $(= m_p a)$ and the force due to the acceleration of the hydrodynamic mass F_{mh} $(= m_h a)$. The hydrodynamic mass m_h can be modelled as the sum of the time independent added mass term and a time dependent term that accounts for the mass entrainment; see Grift *et al.* (2019) for details. Figure 2 shows the theoretical time independent acceleration forces and the steady state force with respect to the measured force signals.

Table 1. Accelerations a and final velocities V considered in the experiments. Black dots indicate the combinations of acceleration and velocity that were possible given the dimensions of the tank. This work shows the results for $V = 0.45$ m/s. Accelerations in italic are excluded from velocity measurements.

		a [m/s^2]									
		0.10	*0.14*	0.21	0.41	0.62	0.82	1.03	1.23	1.44	1.64
V [m/s]	0.15	•	•	•	•	•	•	•	•	•	•
	0.30	•	•	•	•	•	•	•	•	•	•
	0.45	•	•	•	•	•	•	•	•	•	•
	0.60			•	•	•	•	•	•	•	•
	0.75				•	•	•	•	•	•	•
	0.90				•	•	•	•	•	•	•
	1.05					•	•	•	•	•	•
	1.20						•	•	•	•	•
	1.35									•	•

Since Figure 2 shows that the peak force is significantly higher than this theoretical force we divert from this theory of hydrodynamic mass and focus on the instationary force F_{IS} acting on the plate as given by:

$$F_{IS}(t) = F_x(t) - \underbrace{m_p a}_{F_{mp}} - \underbrace{\tfrac{1}{2} C_D \rho A V(t)^2}_{F_{CD}}. \tag{2}$$

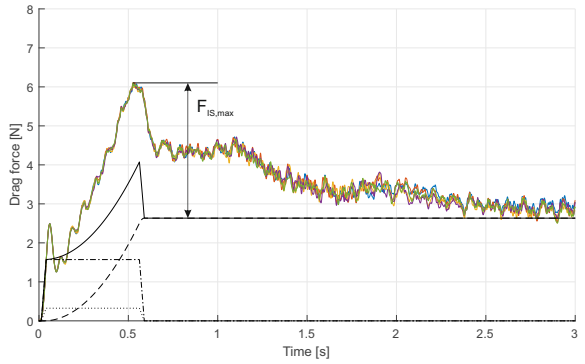

Figure 2. Five repetitions of the force signal $F_x(t)$. Each colored line indicates one repetition of the same experiment with $a = 0.82$ m/s^2 and $V = 0.45$ m/s. The black lines indicate theoretical values: $\ldots : m_p a$, plate mass acceleration force; $-.- : m_p a + m_h a$, plate mass + added mass acceleration force with m_h according to Payne (1981); $- - - : \frac{1}{2} C_D \rho A V^2$, steady state drag force; $- : (\frac{1}{2} C_D \rho A V^2 + m_p a + m_h a)$.

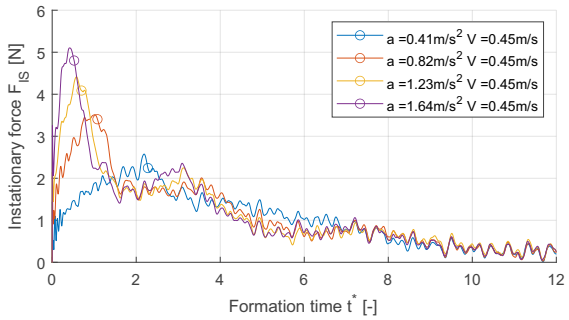

Figure 3. The instationary drag coefficient as a function of the formation time t^* for four different accelerations towards a final velocity of 0.45 m/s. Circles indicate the end of the acceleration phase of each measurement.

The calculation of this instationary force from the experimental data for four different accelerations towards a final velocity of 0.45 m/s leads to Figure 3. Time is made dimensionless by using the formation time (Gharib *et al.*, 1998), which is given by:

$$t^* = \frac{\int_0^t V(\tau)\mathrm{d}\tau}{\ell_b}, \tag{3}$$

which in the present experiment is equivalent to the number of plate heights the plate has travelled. The instationary force is made dimensionless using

$$C_{D,IS} = \frac{F_{IS}}{\frac{1}{2}\rho A V^2}. \tag{4}$$

Figure 3 shows that shortly after the acceleration ended, the different force signals collapse on one curve. It is also seen that the peak instationary force increases with acceleration, which is also expected from the theory of hydrodynamic mass. Figure 4 shows the value of the peak instationary force $F_{IS,max}$

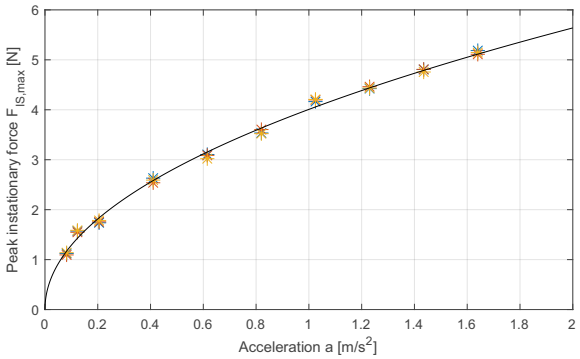

Figure 4. The value of the peak instationary force $F_{IS,max}$, as indicated in Figure 2, as a function of the acceleration. Stars represent multiple realisations of the experiment at different accelerations towards a final velocity of 0.45 m/s This peak force shows an increasing trend with increasing acceleration, following the fitted function $F_{IS,max} = 4.0a^{0.5}$, indicated by the black line.

across the whole range of accelerations. The least-squares fitted function through the data points in Figure 4 is given by $F_{IS,max} = C_1 \cdot a^{0.5}$, with: $C_1 = 4.0$, which is similar to the results of Fernando *et al.* (2020). We also found this scaling, i.e $F_{IS,max} = C_1 \cdot a^{0.5}$ in experiments where the plate accelerates towards different final velocities. The value of the prefactor C_1 depends on the final velocity, size and other characteristics of the plate. This scaling goes against classical added mass theories, which state that the drag force due to acceleration should be linear in the magnitude of the acceleration; see for instance Payne (1981).

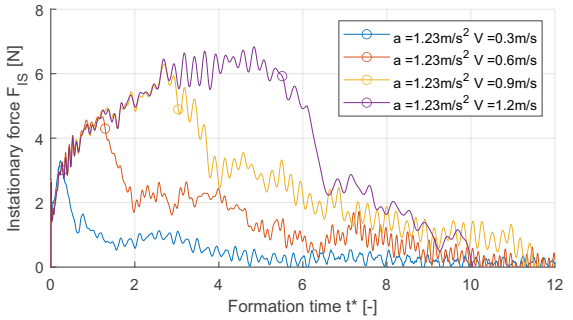

Figure 5. The instationary drag force as a function of the formation time t^* for four measurements with the same acceleration $a = 1.23$ m/s^2 towards four different final velocities. Circles indicate the end of the acceleration phase of each measurement.

The same analysis was done for experiments towards different final velocities, but with the same acceleration. Figure 5 shows the instationary drag force signals for experiments with equal acceleration ($a = 1.23$ m/s^2) towards four different velocities. Contrary to the cases for different accelerations towards the same final velocity, the different signals did not coincide after the acceleration ended. However, the different lines coincide while accelerating, which comes from the fact that when the plate is still accelerating, these experiments are

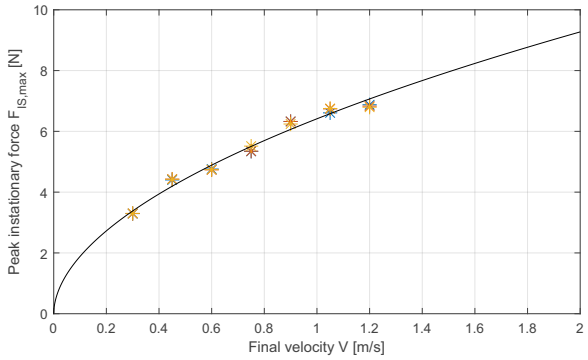

Figure 6. The value of the peak instationary force $F_{IS,max}$, as indicated in Figure 2, as a function of the final velocity V. Stars represent multiple realisations of the experiment with an acceleration of 1.23 m/s^2 towards different final velocities. This peak force shows an increasing trend with increasing final velocity, following the fitted function $F_{IS,max} = 6.4V^{0.5}$, indicated by the black line.

basically the same. The peak instationary force increased with increasing velocity. Figure 6 shows the value of the peak instationary force across the range of final velocities V that could be reached with an acceleration $a = 1.23$ m/s^2. The least-squares fitted function through the data points in Figure 6 is given by $F_{IS,max} = C_2 \cdot V^{0.5}$, with: $C_2 = 6.4$.

Combining the above results gives a first indication that scaling the drag force as in Equation 4 is not ideal for experiments with an accelerating plate. Figure 7 shows multiple measurements (including the experiments from Fernando *et al.* (2020)) and fitted functions similar to Figure 4, but towards different final velocities. In Figure 7 the acceleration was made dimensionless using the acceleration modulus $a^* = \frac{a\ell_b}{V^2}$ and the peak instationary drag force F_{IS} was made dimensionless as in Equation 4. Figure 7 shows that the different curves do not collapse on the same curve, but a clear trend is visible, where results of measurements towards higher velocities are located lower in the graph. Figure 7 also shows the experimental data from Fernando *et al.* (2020), which compares very well to our results. The differences can be explained by the difference in plate geometry between the experiments (rectangular with an aspect ratio of 2 in this study, circular in the experiments of Fernando *et al.* (2020)).

Since the instationary force is proportional to both $a^{0.5}$ and $V^{0.5}$ as in $F_{IS} \sim (aV)^{1/2}$, we propose the following scaling:

$$F^*_{IS} = \frac{F_{IS}}{\rho A(\nu a V)^{1/2}}. \tag{5}$$

Contrary to Equation 4, this new scaling law takes both the acceleration and the viscosity of the fluid into account, even though the Reynolds number for these flow is generally very large. This scaling is also found analytically for the viscous force in Stokes' first problem of the starting plate, when the acceleration is finite instead of impulsively started, using the diffusion equations given by Crank (1975) on linearly increasing boundary conditions. Figure 8 shows the same peak instationary forces $F_{IS,max}$ as Figure 7, but here $F_{IS,max}$ is made dimensionless with the proposed scaling given in Equation 5. Figure 8 shows that the peak instationary forces collapse significantly better than in Figure 7.

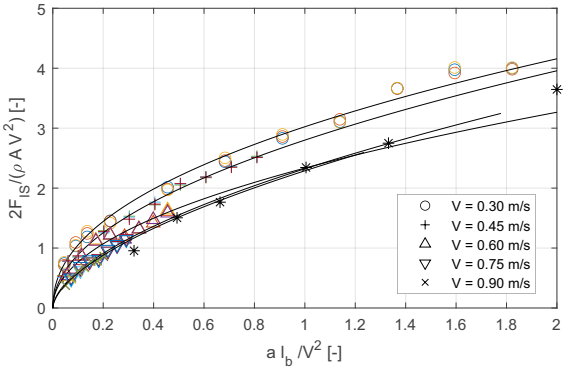

Figure 7. The peak instationary force $F_{IS,max}$ as a function of the acceleration, similar to Figure 4, for different final velocities. The force is made dimensionless using Equation 4, the acceleration is made dimensionless using the acceleration modulus $a^* = \frac{a\ell_b}{V^2}$. Black lines indicate the fitted function to each set of measurements towards the same final velocity. The black stars indicate the experiments from Fernando *et al.* (2020).

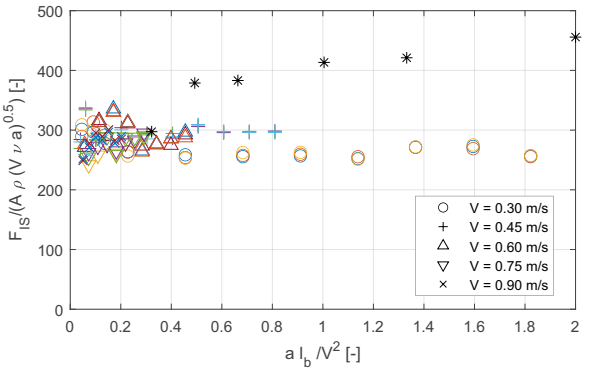

Figure 8. The peak instationary force $F_{IS,max}$ as a function of the acceleration, similar to Figure 4, for different final velocities. The force is made dimensionless using Equation 5, the acceleration is made dimensionless using the acceleration modulus $a^* = \frac{a\ell_b}{V^2}$. All values lie around 300, with a maximum deviation of 15 percent. The black stars indicate the experiments from Fernando *et al.* (2020), which deviate from our experiments, due to the difference in plate geometry

VELOCITY MEASUREMENTS

For each time step the dimensionless vorticity ω^* was determined from the instantaneous velocity fields as in:

$$\omega^* = \frac{\omega \ell_b}{V}. \tag{6}$$

Then, the dimensionless circulation Γ^* is calculated from:

$$\Gamma^* = \int_{S^*} \omega^* \mathrm{d}S^*, \tag{7}$$

where S^* is the area over which the integration takes place, which is made dimensionless with ℓ_b. Since the flow field is symmetric over the field-of-view during the experiment, the net circulation should be zero. Therefore the circulation

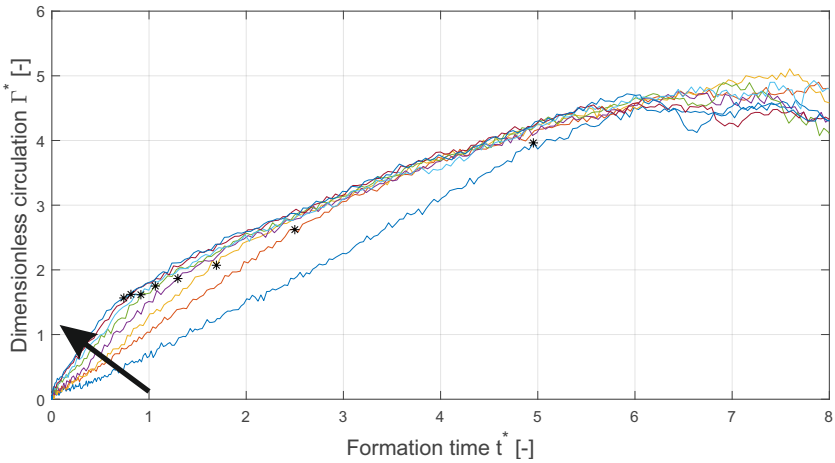

Figure 9. Dimensionless circulation Γ^* over the top half of the field-of-view as a function of the formation time t^* towards a final velocity of 0.45 m/s. Different colored lines indicate accelerations between $a = 0.21$ m/s^2 and $a = 1.64$ m/s^2 (see Table 1), with increasing acceleration following the arrow. Black stars indicate the end of the acceleration phase. Shortly after the end of the acceleration phase the lines collapse onto the same line. Vortex breakup occurs at $t^* \simeq 6$.

in Figure 9 is calculated over the top half of the field-of-view. Plotting the circulation against the formation time in Figure 9 shows that the circulation initially increases faster with higher accelerations. However, when the acceleration phase has ended, the circulation increases at a lower rate and coincides with the circulation for higher accelerations. When the formation time reaches $t^* \simeq 6$, the vortices break up (Grift *et al.*, 2019), which is clearly seen in Figure 9 by the drop in circulation and the divergence of the lines.

Figure 10 shows the vorticity fields at four different formation times ($t^* = 0.75$, 2.0, 4.0 and 7.5) and four different accelerations ($a = 0.21$, 0.62 1.03 and 1.64 m/s^2). It can be seen that the shapes and locations of the initial primary vortices at $t^* = 0.75$ and $t^* = 2$ are very similar for all accelerations with only a difference in the strength of the vortices. These vorticity fields compare very well to the numerical results of Koumoutsakos & Shiels (1996) and the experiments of Fernando & Rival (2016). For all accelerations the initial shear layer development, starting at the edge of the plate, is very similar. From the shear layer secondary vortices are formed that merge with the primary vortex. This process is visualized by Grift *et al.* (2019), and is in line with the framework for start-up vortices proposed by Luchini & Tognaccini (2002). Further into the plate motion, at $t^* = 4$, there are clear differences between the vorticity fields of the lower accelerations (0.21 and 0.62 m/s^2) and the higher accelerations (1.03 and 1.64 m/s^2). The higher accelerations show clear regions of high vorticity close the plate, which are not present at the lower accelerations. This is especially surprising for the case with $a = 0.62$ m/s^2, since Figure 10 shows that the circulation of this case is equal to the cases with higher accelerations. The vorticity fields at $t^* = 7.5$ show less similarities, since vortex break-up has already occurred when $t^* \simeq 6$ and a turbulent wake is present, which resembles the steady state turbulent wake. Further research will be done on the vortex build-up close to the plate as seen at $t^* = 4$, and how the vorticity fields will look like when acceleration is prolonged to higher final velocities.

CONCLUSIONS

The present study shows the results of the experiments on a starting flat plate in a water tank, accelerated from rest by an industrial gantry robot. We measured both the drag force acting on and the velocity fields surrounding the plate for a wide range of accelerations and final velocities. It is found that adding the hydrodynamic mass force to the steady state force significantly underestimates the instantaneous drag force measured in the experiments, both during the acceleration as well as in the period after the acceleration. Instead of added mass we proposed an instationary force that scales with the square root of both the acceleration and the velocity. This scaling can predict the instationary force significantly better than the conventional scaling given in Equation 4, which does not take the magnitude of the acceleration into account.

The vorticity fields showed the same process of vortex formation during the acceleration period as a function of the formation time up to a formation time of 6, after which the vortices break up. The circulation during the acceleration period differed for different accelerations, but coincided on the same curve shortly after the circulation had ended.

In future work we will test the new scaling law we found on different objects to see if it is also valid in other cases, and investigate the underlying physics of it further to determine a more general scaling law that is valid for other cases, such as higher accelerations or non-constant accelerations.

Acknowledgement

This work is part of the 'ImpulsiveFlows' project that has received funding from the European Research Council (ERC) under the European Union's Horizon 2020 research and innovation programme (Grant agreement No. 884778).

REFERENCES

Crank, J. 1975 *The mathematics of diffusion*, 2nd edn. Oxford, Eng: Clarendon Press.

Fernando, J.N., Weymouth, G.D. & Rival, D.E. 2020 On the limits of added-mass theory in separated flows and with varying initial conditions. *Journal of Fluids and Structures* **93**, 102835.

Fernando, J. N. & Rival, D. E. 2016 On vortex evolution in the wake of axisymmetric and non-axisymmetric low-aspect-ratio accelerating plates. *Phys. Fluids* **28** (1), 017102.

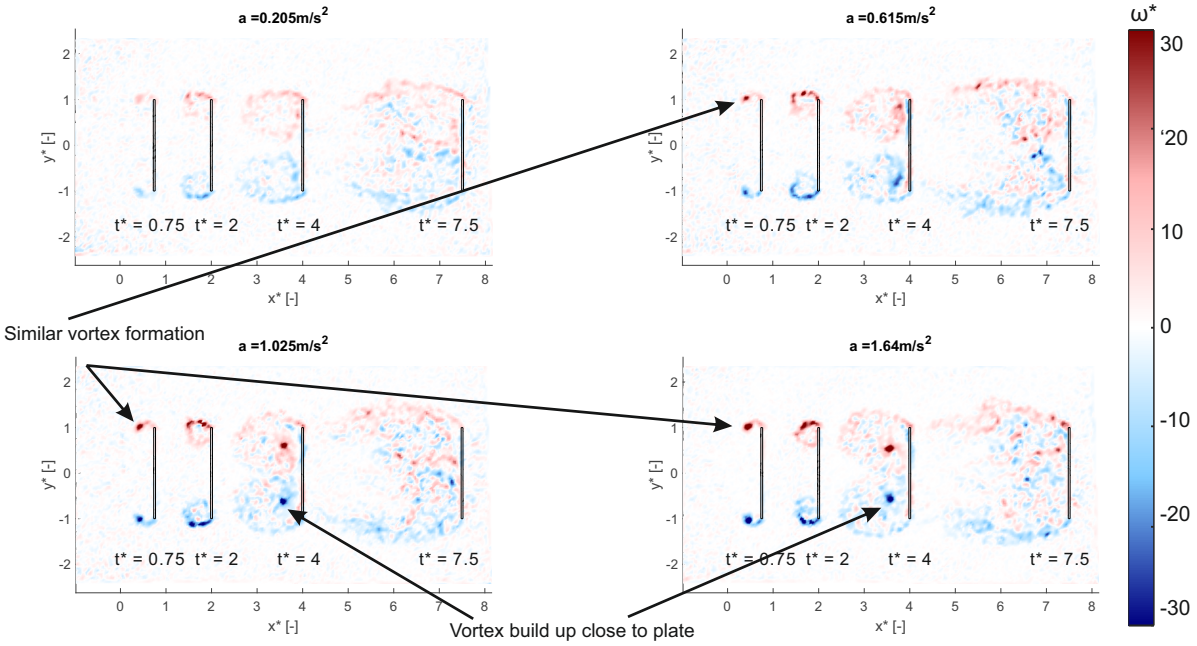

Figure 10. Dimensionless vorticity fields at different formation times t^* for four different accelerations towards the final velocity $V = 0.45\mathrm{m/s}$. Integration of vorticity over the top half of these pictures for each time step results in Figure 9. The formation of vortices from the shear layer shows a similar behaviour at low formation times, with increasing vortex strength for increasing acceleration. At $t^* = 4$, all except the lowest acceleration have equal circulation, but only the two higher acceleration show similar vortex growth near the mid plane of the plate. At $t^* = 6$, vortex break-up has occurred and the vorticity fields at $t^* = 7.5$ shows more chaotic, turbulent behaviour. Note: x^* is equivalent to t^* in this figure.

Gharib, M., Rambod, E. & Shariff, K. 1998 A universal time scale for vortex ring formation. *J. Fluid Mech.* **360**, 121–140.

Grift, E. J., Vijayaragavan, N. B., Tummers, M. J. & Westerweel, J. 2019 Drag force on an accelerating submerged plate. *J. Fluid Mech.* **866**, 369–398.

Koumoutsakos, P. & Shiels, D. 1996 Simulations of the viscous flow normal to an impulsively started and uniformly accelerated flat plate. *J. Fluid Mech.* **328**, 177–227.

Leonard, A. & Roshko, A. 2001 Aspects of flow-induced vibration. *Journal of Fluids and Structures* **15** (3), 415–425.

Luchini, P. & Tognaccini, R. 2002 The start-up vortex issuing from a semi-infinite flat plate. *J. Fluid Mech.* **455**, 175–193.

Mancini, P., Manar, F., Granlund, K., Ol, M. V. & Jones, A. R. 2015 Unsteady aerodynamic characteristics of a translating rigid wing at low reynolds number. *Physics of Fluids* **27** (12), 123102.

Mulleners, K., Mancini, P. & Jones, A.R. 2017 Flow development on a flat-plate wing subjected to a streamwise acceleration. *AIAA Journal* **55** (6), 2118–2122.

Payne, P. R. 1981 The virtual mass of a rectangular flat-plate of finite aspect ratio. *Ocean Eng.* **8** (5), 541–545.

Rival, D., Prangemeier, T. & Tropea, C. 2009 The influence of airfoil kinematics on the formation of leading-edge vortices in bio-inspired flight. *Experiments in Fluids* **46** (5), 823–833.

Weymouth, G. D. & Triantafyllou, M. S. 2013 Ultra-fast escape of a deformable jet-propelled body. *Journal of Fluid Mechanics* **721**, 367–385.